Intraseasonal Variation of Winter Precipitation over the Western United States Simulated by 14 IPCC AR4 Coupled GCMs

JIA-LIN LIN,* TOSHIAKI SHINODA,+ TAOTAO QIAN,*,# WEIQING HAN,@ PAUL ROUNDY,& AND YANGXING ZHENG**

* *Department of Geography, The Ohio State University, Columbus, Ohio*
+ *Naval Research Laboratory, Stennis Space Center, Mississippi*
# *Byrd Polar Research Center, The Ohio State University, Columbus, Ohio*
@ *Department of Atmospheric and Oceanic Sciences, University of Colorado, Boulder, Colorado*
& *University at Albany, State University of New York, Albany, New York*
** *NOAA/ESRL/CIRES Climate Diagnostics Center, Boulder, Colorado*

(Manuscript received 18 November 2008, in final form 16 June 2009)

ABSTRACT

This study evaluates the intraseasonal variation of winter precipitation over the western United States in 14 coupled general circulation models (GCMs) participating in the Intergovernmental Panel on Climate Change (IPCC) Fourth Assessment Report (AR4). Eight years of each model's twentieth-century climate simulation are analyzed. The focus is on the two dominant intraseasonal modes for the western U.S. precipitation: the 40-day mode and the 22-day mode.

The results show that the models tend to overestimate the northern winter (November–April) seasonal mean precipitation over the western United States and Canada. The models also tend to produce overly strong intraseasonal variability in western U.S. wintertime precipitation, in spite of the overly weak tropical intraseasonal variability in most of the models. All models capture both the 40-day mode and the 22-day mode, usually with overly large variances. For the 40-day mode, models tend to reproduce its deep barotropic vertical structure and three-cell horizontal structure, but only 5 of the 14 models capture its northward propagation, and only 2 models simulate its teleconnection with the Madden–Julian oscillation in the tropical Pacific. For the 22-day mode, 8 of the 14 models reproduce its coherent northward propagation, and 9 models capture its teleconnection with precipitation in the tropical Pacific.

1. Introduction

The western United States normally receives the bulk of its precipitation during Northern Hemisphere (NH) winter from October to April, when the storm track across the North Pacific is active (e.g., Mo and Nogues-Paegle 2005). Rainfall in the western United States during this season is significantly modulated on the intraseasonal time scale (Mo and Higgins 1998a,b; Mo 1999). For example, alternating wet and dry episodes with periods around 20 days are often observed at coastal stations in California (Mo 1999), and strong flooding in California is often associated with rainfall events on the submonthly time scale (e.g., Mo and Nogues-Paegle 2005).

Mo (1999) demonstrated that the intraseasonal variability of western U.S. winter precipitation has two dominant modes: a mode with a period of about 36–40 days (hereafter the 40-day mode) and a mode with a period of about 20–25 days (hereafter the 22-day mode). Previous studies have found four mechanisms for generating the intraseasonal variability of western U.S. winter precipitation (Fig. 1): 1) instability of the basic state (e.g., Simmons et al. 1983; Schubert 1986; Frederiksen 1986; Dole and Black 1990; Schubert et al. 1993), 2) orographic forcing (Marcus et al. 1994, 1996), 3) interactions with synoptic-scale eddies (Lau 1988; Held et al. 1989), and 4) forcing of tropical convection (Mo and Higgins 1998a, 1998b, Mo 1999). Of particular importance for extended-range weather forecasts is the tropical forcing mechanism. As shown by Mo (1999), the 40-day mode is related to the Madden–Julian oscillation (MJO) in the tropics,

Corresponding author address: Dr. Jia-Lin Lin, Dept. of Geography, The Ohio State University, 1105 Derby Hall, 154 North Oval Mall, Columbus, OH 43210.
E-mail: lin.789@osu.edu

DOI: 10.1175/2009JCLI2991.1

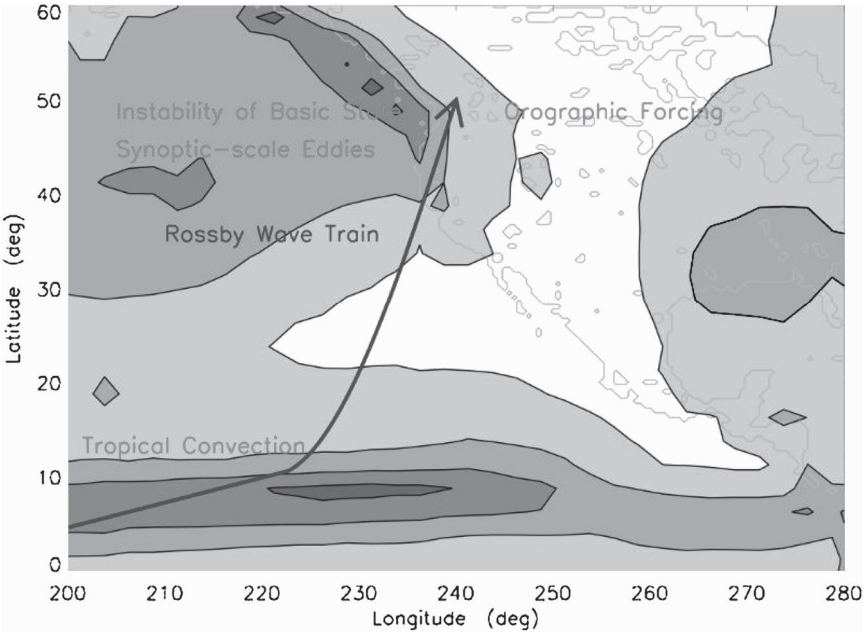

FIG. 1. Schematic depiction of the suggested mechanisms for the intraseasonal variability of western U.S. winter precipitation. Contour is the northern winter (November–April) seasonal mean GPCP precipitation. The first contour is 1 mm day^{-1}, and the contour interval is 2 mm day^{-1}. The black arrow schematically shows that these modes are propagated from the tropical Pacific.

with enhanced convection propagating from the western Pacific to the central Pacific. The spatial structure of precipitation anomaly excited by the propagation of convection exhibits a north–south three-sell pattern. Heavy precipitation in California is associated with dry conditions over Washington; British Columbia, Canada; and along the southeastern coast of Alaska and reduced precipitation over the subtropical eastern Pacific (Mo and Higgins 1998a). When enhanced convection moves to the central Pacific, the response in the Northern Hemisphere resembles the Pacific–North American (PNA) teleconnection pattern (Wallace and Gutzler 1981; Weickmann et al. 1985; Knutson and Weickmann 1987). The 22-day mode is also related to tropical convection with cloud bands propagating northward along the west coast of North America from the eastern Pacific through California to the Pacific Northwest. The spatial structure of this mode is similar to the traveling pattern described by Branstator (1987).

These intraseasonal modes are responsible for alternating wet and dry episodes over the western United States. However, only a few previous studies have examined their simulations by the general circulation models (GCMs). In a pioneering study, Schubert et al. (1993) examined the simulations by an atmospheric GCM developed at the National Aeronautics and Space Administration (NASA) Goddard Laboratory for Atmospheres. They found that the GCM's leading mode in the upper-tropospheric zonal wind is associated with fluctuations of the East Asian jet; this mode resembles the structure of the PNA pattern found in the observations on these time scales. The GCM produces 60% of the total observed Pacific sector low-frequency zonal wind variance. About one-third of the missing variability appears to be due to unrealistic simulations of the MJO.

Recently, in preparation for the Intergovernmental Panel on Climate Change (IPCC) Fourth Assessment Report (AR4), more than a dozen international climate modeling centers conducted a comprehensive set of long-term simulations for both the twentieth century's climate and different climate change scenarios in the 21st century (Randall et al. 2007). Before conducting the extended simulations, many of the modeling centers applied an overhaul to their physical schemes to incorporate the state-of-the-art research results. For example, almost all modeling centers have implemented prognostic cloud microphysics schemes to their models, some have added a moisture trigger to their deep convection schemes, and some now take into account convective momentum transport. Moreover, many modeling centers increased their models' horizontal and vertical resolutions, and some conducted experiments with different resolutions.

TABLE 1. List of models included in this study. For downdrafts, saturated convective downdrafts are denoted SC, unsaturated convective downdrafts are UC, and mesoscale downdrafts are Meso. CAPE means convective available potential energy.

Modeling groups	IPCC identification (label in figures)	Grid type/resolution/model top	Deep convection scheme/modification	Downdrafts SC/UC/Meso	Closure/trigger
NOAA/Geophysical Fluid Dynamics Laboratory	GFDL-CM2.0 (GFDL2.0)	Grid point 144 × 90 L24 3 mb	Moorthi and Suarez (1992); Tokioka et al. (1988)	N/N/N	CAPE/threshold
NOAA/Geophysical Fluid Dynamics Laboratory	GFDL-CM2.1 (GFDL2.1)	Grid point 144 × 90 L24 3 mb	Moorthi and Suarez (1992); Tokioka et al. (1988)	N/N/N	CAPE/threshold
National Center for Atmospheric Research	CCSM3 (CCSM3)	Spectral T85 × L26 2.2 mb	Zhang and McFarlane (1995)	Y/N/N	CAPE
National Center for Atmospheric Research	PCM (PCM)	Spectral T42 × L26 2.2 mb	Zhang and McFarlane (1995)	Y/N/N	CAPE
NASA Goddard Institute for Space Studies	GISS-AOM (GISS-AOM)	Grid point 90 × 6 L12	Russell et al. (1995)	N/N/N	CAPE
NASA Goddard Institute for Space Studies	GISS-ER (GISS-ER)	Grid point 72 × 46 L20 0.1 mb	Del Genio and Yao (1993)	Y/N/N	Cloud-base buoyancy
Center for Climate System Research, National Institute for Environmental Studies, and Frontier Research Center for Global Change	MIROC3.2–hires (MIROC-hires)	Spectral T106 × L56	Pan and Randall (1998); Emori et al. (2001)	Y/N/N	CAPE/relative humidity
Same as above	MIROC3.2-medres (MIROC-medres)	Spectral T42 × L20 30 km	Pan and Randall (1998); Emori et al. (2001)	Y/N/N	CAPE/relative humidity
Meteorological Research Institute	MRI-CGCM2.3.2 (MRI)	Spectral T42 × L30 0.4 mb	Pan and Randall (1998)	Y/N/N	CAPE
Canadian Centre for Climate Modeling and Analysis	CGCM3.1-T47 (CGCM)	Spectral T47 × L32 1 mb	Zhang and McFarlane (1995)	Y/N/N	CAPE
Max Planck Institute for Meteorology	ECHAM5/MPI-OM (MPI)	Spectral T63 × L31 10 mb	Tiedtke (1989); Nordeng (1994)	Y/N/N	CAPE/moisture convergence
Institute Pierre Simon Laplace	IPSL-CM4 (IPSL)	Grid point 96 × 72 L19	Emanuel (1991)	Y/Y/N	CAPE
Météo-France/Centre National de Recherches Météorologiques	CNRM-CM3 (CNRM)	Spectral T63 × L45 0.05 mb	Bougeault (1985)	N/N/N	Kuo (1974)
CSIRO Atmospheric Research	CSIRO Mk3.0 (CSIRO)	Spectral T63 × L18 4 mb	Gregory and Rowntree (1990)	Y/N/N	Cloud-base buoyancy

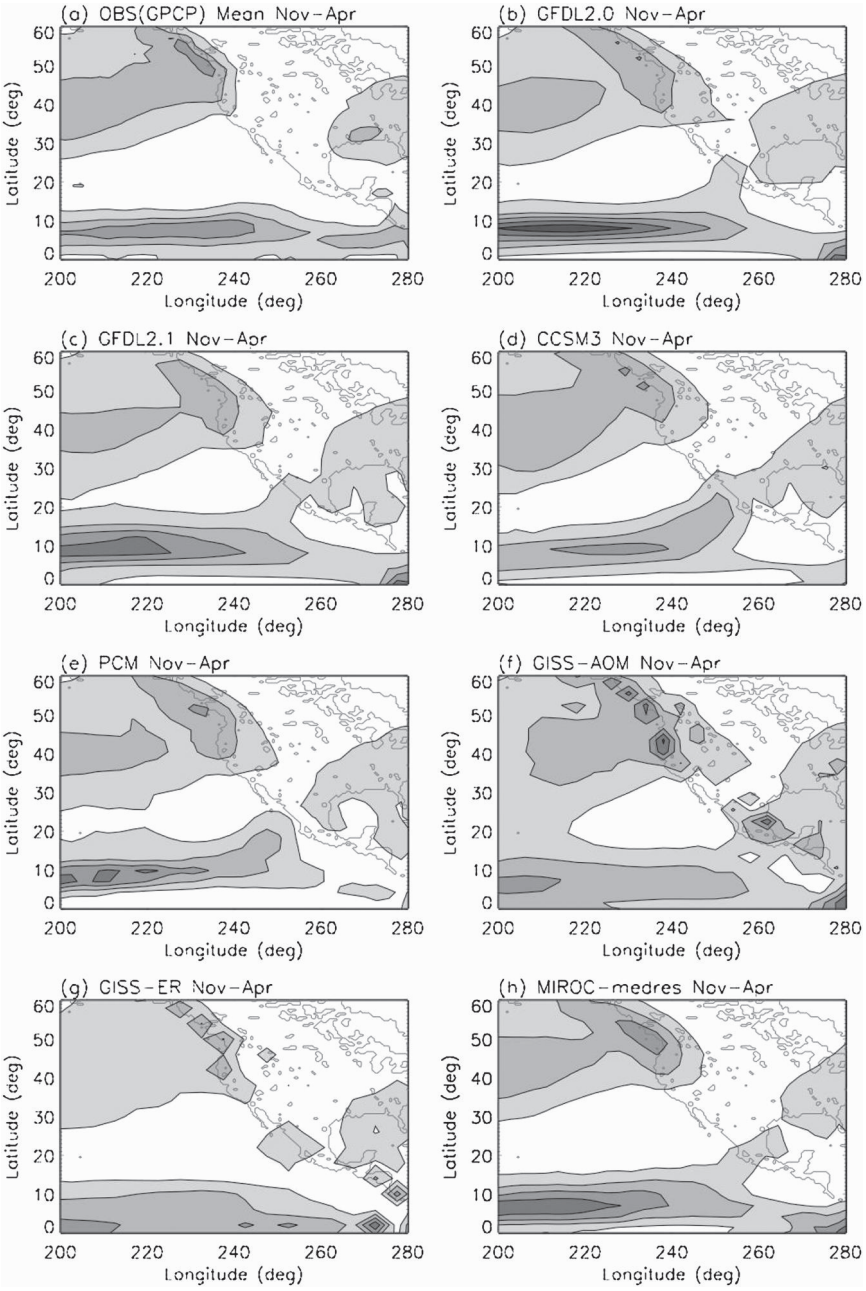

FIG. 2. Northern winter (November–April) seasonal mean precipitation for (a) observation and (b)-(h) the 14 IPCC AR4 models. The first contour is 2 mm day^{-1}, and the contour interval is 2 mm day^{-1}.

The purpose of this study is to evaluate the intraseasonal variation of winter precipitation over the western United States in 14 IPCC AR4 coupled GCMs, with emphasis on the 40-day mode and the 22-day mode. The models and validation datasets used in this study are described in section 2. The diagnostic methods are described in section 3. Results are presented in section 4. A summary and discussion are given in section 5.

2. Models and validation datasets

This analysis is based on 8 yr of the Climate of the Twentieth Century (20C3M) simulations from 14 coupled GCMs. Table 1 shows the model names and acronyms, their horizontal and vertical resolutions, and brief descriptions of their deep convection schemes. For each model we used 8 yr of daily mean surface precipitation.

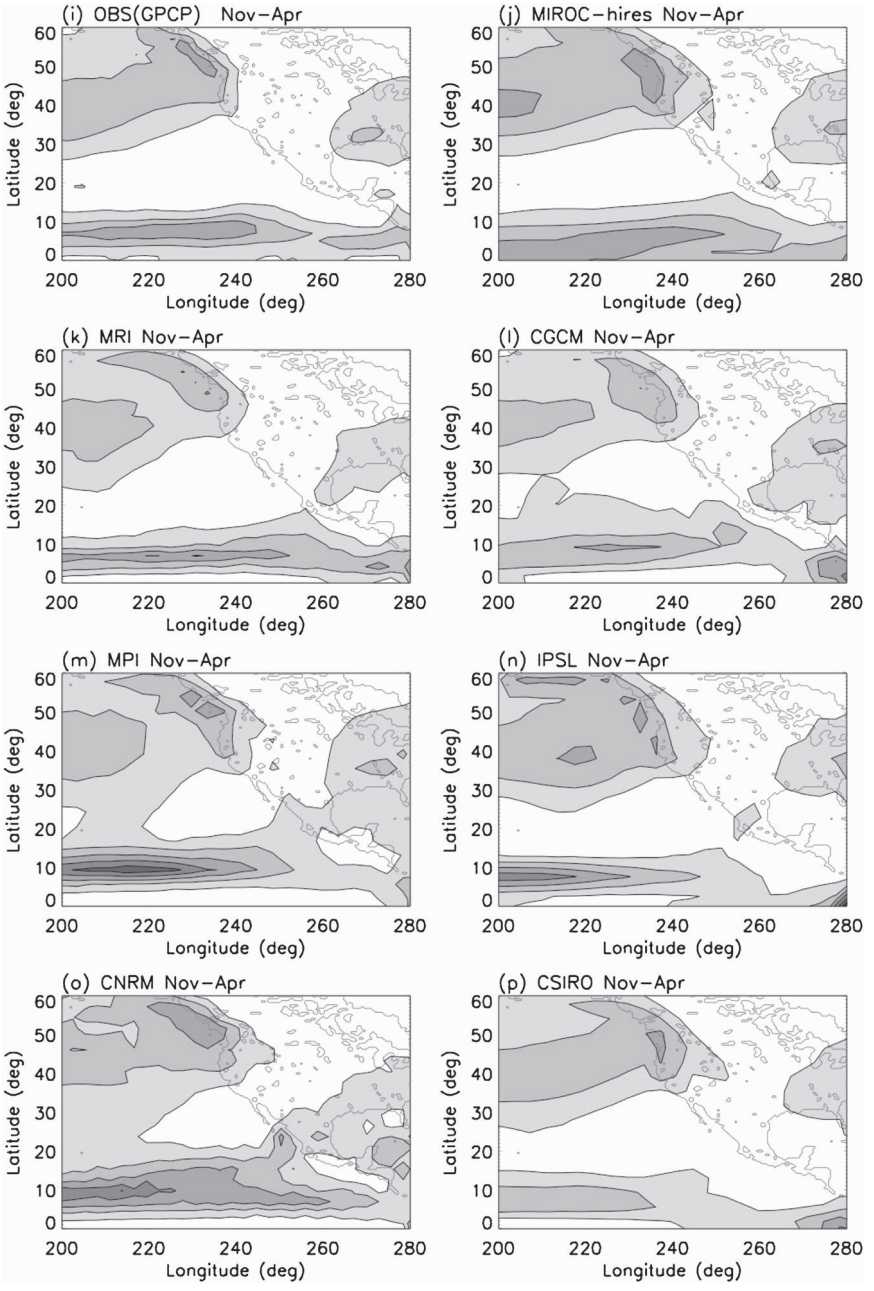

FIG. 2. (*Continued*)

Three-dimensional data are available for 7 of the 14 models, for which we analyzed upper air winds, temperature, and specific humidity.

The model simulations were validated using the Global Precipitation Climatology Project (GPCP) Version 2 Precipitation (Huffman et al. 2001). We used 8 yr (1997–2004) of daily data with a horizontal resolution of 1° longitude × 1° latitude. Obtaining reliable precipitation estimates, especially over the open ocean area where surface observations are sparse, continues to be a big challenge for the research community and was the motivation for the international GPCP project. The GPCP dataset is a merged analysis incorporating available precipitation estimates from low-orbit-satellite microwave data, geosynchronous-orbit-satellite infrared data, and rain gauge observations. Gruber and Levizzani (2008) provided a detailed assessment of the GPCP dataset. The data quality varies significantly from region to region.

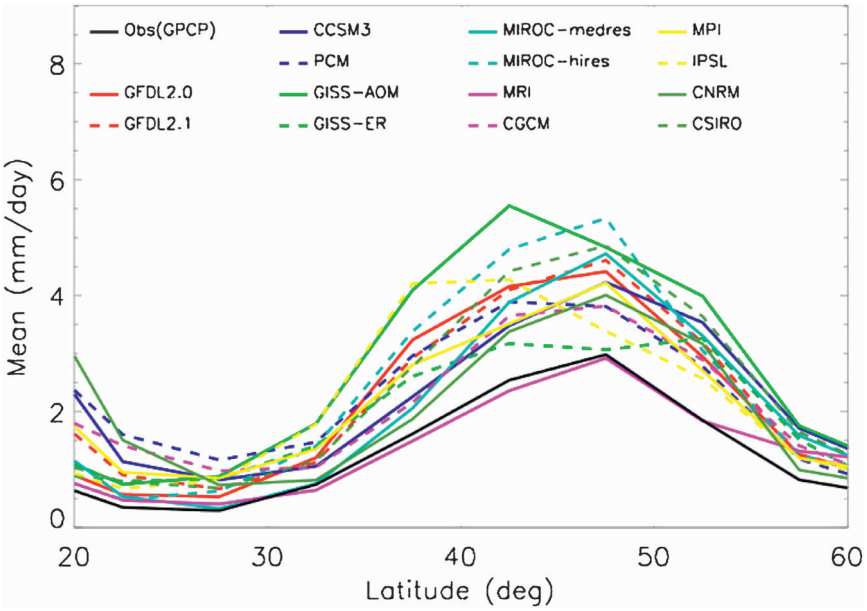

FIG. 3. Meridional profile of northern winter (November–April) seasonal mean precipitation (mm day^{-1}) averaged between 125° and 115°W for observation and 14 models.

Fortunately, the region of interest for this study (the western United States and surrounding regions) is associated with relatively good data quality, although substantial uncertainties still exist (see Fig. 2.2 of Gruber and Levizzani 2008).

To evaluate the model-simulated atmospheric circulation, we also used 8 yr (1997–2004) of daily National Centers for Environmental Prediction (NCEP) reanalysis data (Kalnay et al. 1996), for which we analyzed upper air winds, temperature, and specific humidity. There are possible errors associated with the reanalysis data coming from measurement errors, poor data coverage over certain geographical regions, and effects of assimilation models. However, previous studies have shown that the errors could be significantly reduced by spatial averaging over many grid points and constructing a composite over many events (e.g., Carr and Bretherton 2001; Lin et al. 2005, 2008).

3. Methods

Total intraseasonal (periods 10–90 days) anomalies were obtained by applying a 365-point 10–90-day Lanczos filter (Duchan 1979). Because the Lanczos filter is nonrecursive, 182 days of data were lost at each end of the time series (364 days in total). The dominant intraseasonal modes are determined using wavelet spectra because they are active mainly during the southern summer. Wavelet spectrum is a powerful tool for analyzing multiscale, nonstationary processes. Its uniqueness is its ability to simultaneously localize the variability of the signal in both the frequency and time domains by using generalized local base functions (wavelets) that can be stretched and translated with a flexible resolution in both frequency and time (e.g., Mak 1995; Torrence and Compo 1998). In other words, one can simultaneously determine both the dominant modes of variability and how those modes vary in time. We utilize the wavelet analysis program developed by Torrence and Compo (1998) and use the Morlet wavelet as the mother wavelet. We have tested different mother wavelets (Paul or Derivative of Gaussian), and the results are similar. The 40-day mode, defined as precipitation variability in the period range of 30–60 days, was obtained by applying a 365-point 30–60-day Lanczos filter. Similarly, the 22-day mode is defined as precipitation variability in the period range of 20–30 days and was obtained by applying a 365-point 20–30-day Lanczos filter. We also tested the Murakami (1979) filter, and the results are similar.

4. Results

a. Northern winter (November–April) seasonal mean precipitation

Previous observational studies indicate that the intraseasonal variance of precipitation is highly correlated with time-mean precipitation (e.g., Wheeler and Kiladis 1999). Therefore, we first look at the horizontal distribution of

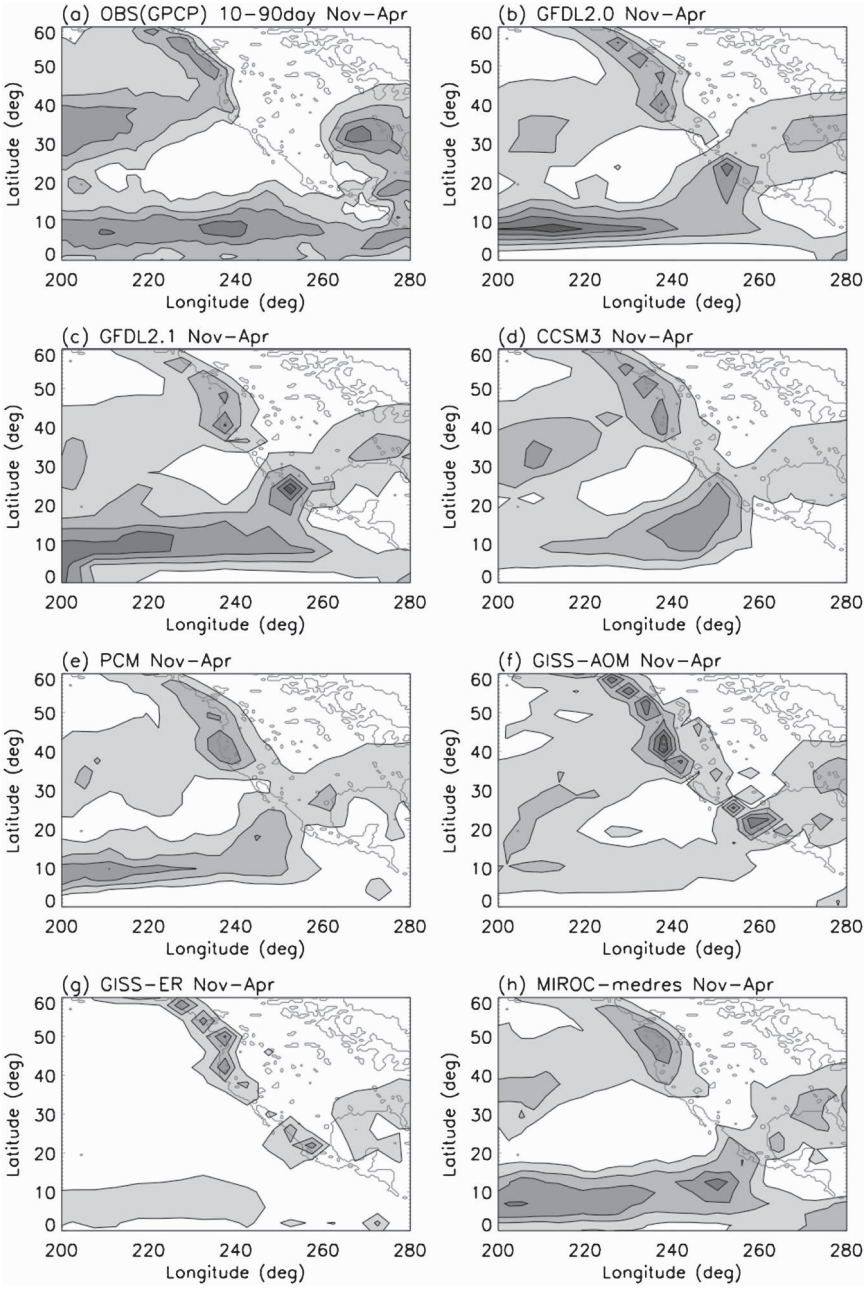

FIG. 4. Horizontal distribution of the standard deviation of total intraseasonal (10–90 day) precipitation anomaly during northern winter (November–April) (a) observation and (b)-(h) the 14 IPCC AR4 models. The first contour is 2 mm day^{-1}, and the contour interval is 1 mm day^{-1}.

northern winter (November–April) seasonal mean precipitation (Fig. 2). If we use the 2 mm day^{-1} contour to define the gross horizontal pattern of precipitation in observation, all 14 models capture reasonably this gross pattern. In particular, they all produce the NE–SW-tilted North Pacific storm track. Most of them also reproduce the peak along the west coast of the United States and Canada. The eastern Pacific ITCZ is also reasonably simulated by all models although with a large variation in precipitation magnitude.

To conduct a more quantitative evaluation of the seasonal mean precipitation over the western United States, we plot in Fig. 3 the meridional profile averaged between 235° and 245°E. There is a wide spread among

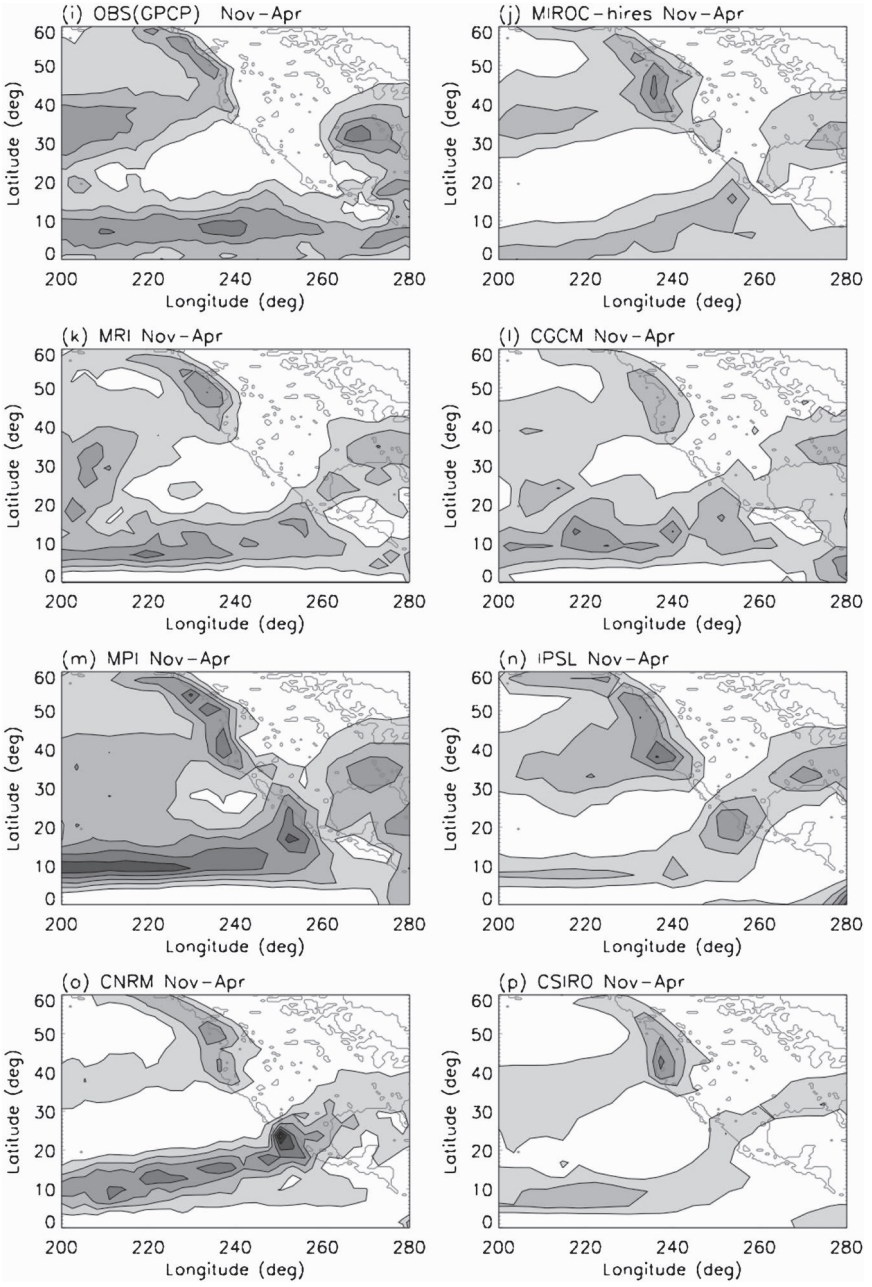

FIG. 4. (*Continued*)

the models. All but two models [the Meteorological Research Institute model (MRI-CGCM2.3.2, hereafter MRI) and the Goddard Institute for Space Studies ER model (GISS-ER)] overestimate the precipitation by more than 30%. The MRI model precipitation is in excellent agreement with observation. The precipitation peak is shifted slightly northward in one model (GISS-ER) but slightly southward in two others [the GISS Atmosphere–Ocean Model (GISS-AOM) and the Institute Pierre Simon Laplace Climate Model version 4 (IPSL-CM4, hereafter IPSL)].

b. Total intraseasonal (10–90 day) variance

Figure 4 shows the horizontal distribution of the total intraseasonal (10–90 day) variance of precipitation during northern winter (November–April). In observation (Fig. 4a), the horizontal distribution of total intraseasonal variance follows that of seasonal mean precipitation

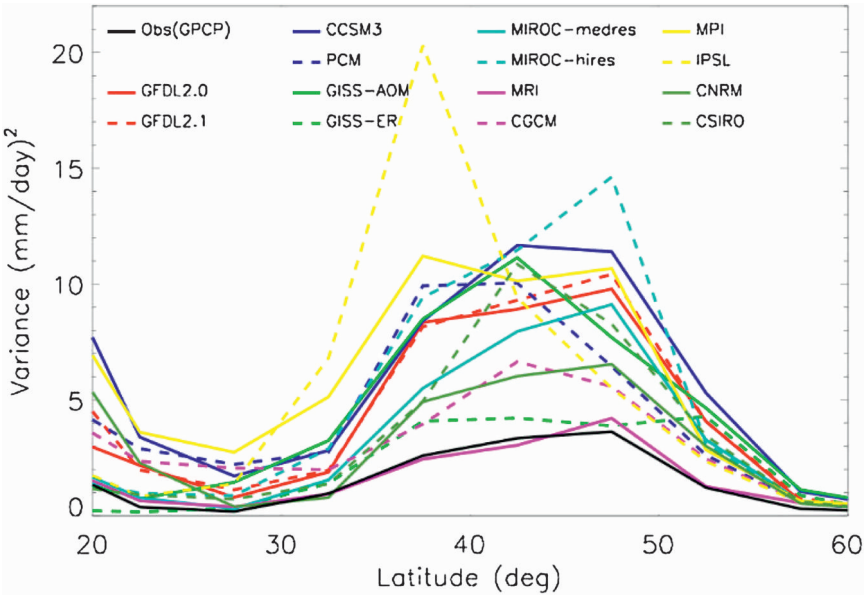

FIG. 5. Meridional profile of the total intraseasonal (10–90 day) variance (mm^2 day^{-2}) of precipitation anomaly averaged between 125° and 115°W.

(Fig. 2), except that the variance over the North Pacific storm track is shifted slightly southward compared to the seasonal mean precipitation. The model variances show three characteristics. First, all models capture the basic spatial pattern of the variance, including the slight southward shift compared to the seasonal mean precipitation. Second, most models produce overly large variance along the west coast of the United States and Canada. Third, all models underestimate the variance over the North Pacific Ocean, in spite of the fact that they generally produce reasonable seasonal mean precipitation in that region (Fig. 2). This suggests an interesting land–sea contrast in the models' ability to simulate extratropical intraseasonal variability, with a better performance over land than over ocean.

To provide a more quantitative evaluation of the model simulations, Fig. 5 shows the meridional profile of total intraseasonal (10–90 day) variance of precipitation during northern winter averaged between 125°E and 115°W. Over the western United States and Canada, all but two models (MRI and GISS-ER) produce a variance that is 2–7 times the observed variance, which is consistent with their overly large seasonal mean precipitation (Fig. 3). This is in sharp contrast with the models' simulations of tropical intraseasonal variability (Lin et al. 2006). Although the models generally produce reasonable seasonal mean tropical precipitation, only a few of them could simulate reasonable tropical intraseasonal variability, suggesting that the tropical intraseasonal variability is generated by mechanisms different from the extratropical intraseasonal variability.

c. *The dominant intraseasonal modes*

Figure 6 shows the wavelet spectrum of precipitation averaged between 40°–45°N and 125°–115°W for observation and the 14 IPCC models. The Morlet wavelet was used as the mother wavelet. We have tested different mother wavelets (Paul or Derivative of Gaussian), and the results look similar. The observed spectrum (Fig. 6) demonstrates two dominant intraseasonal modes, a 30–60-day mode (the so-called 40-day mode) and a 15–30-day mode (the so-called 22-day mode). All models capture both modes, and the model variances are generally larger than the observed variances. The models also tend to produce more frequent active episodes.

d. *The 40-day mode*

Next we focus on the 40-day mode. Figure 7 shows the meridional profile of the 40-day mode variance averaged between 125° and 115°W. For both the observation and the models, the spatial distribution of the 40-day mode variance looks quite similar to that of the total intraseasonal variance. All but one model (MRI) produce 2–9 times the observed 40-day mode variance over the western United States and Canada. The MRI model variance is in very good agreement with the observed variance.

Figure 8 shows the lag-correlation of the 40-day mode precipitation anomaly averaged between 125° and 115°W with respect to itself at 37.5°N, 240°E. Shading denotes the regions where lag-correlation is above the 95% confidence level. In observation (Fig. 8a), the 40-day

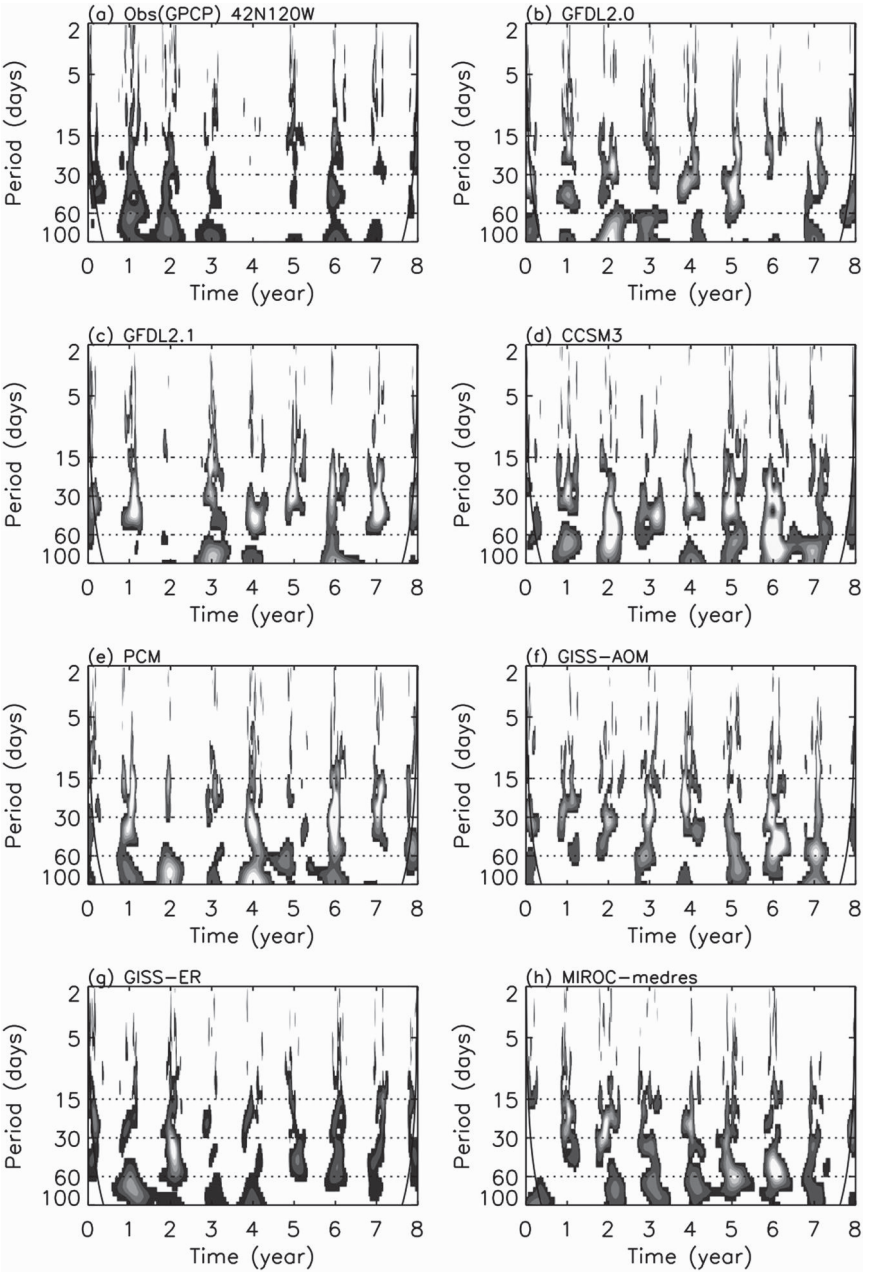

FIG. 6. Wavelet spectrum of precipitation averaged between 40°–45°N, 125°–115°W.

mode propagates northward from 10° to 50°N, which is consistent with the results of Mo (1999). Five of the 14 models simulate coherent northward propagations [the Geophysical Fluid Dynamics Laboratory Climate Model version 2.0 (GFDL-CM2.0, hereafter GFDL2.0), the Community Climate System Model version 3 (CCSM3), MRI, the Canadian Centre for Climate Modeling and Analysis Coupled General Circulation Model (CGCM3.1-T47, hereafter CGCM), and IPSL]. Two models produce standing oscillation [GFDL2.1 and the National Center for Atmospheric Research (NCAR) Parallel Climate Model (PCM)], while the other seven models simulate southward propagations [GISS-AOM, GISS-ER, the Model for Interdisciplinary Research on Climate-medres (MIROC-medres), MIROC-hires, the Max Planck Institute for Meteorology (ECHAM5/MPI-OM, hereafter MPI), the Météo-France/Centre National de Recherches Météorologiques Climate Model version 3 (CNRM-CM3, hereafter CNRM), and the Commonwealth Scientific and Industrial Research

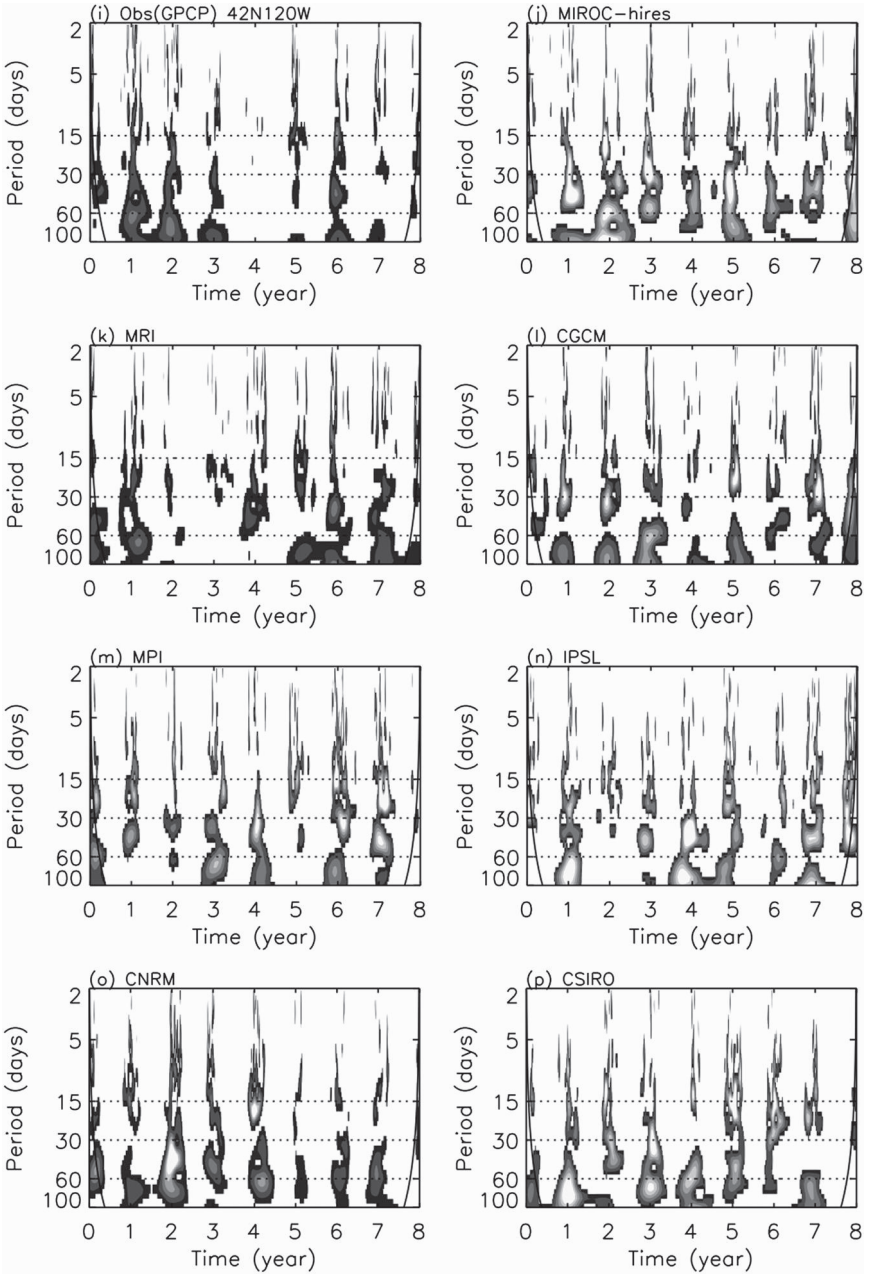

FIG. 6. (*Continued*)

Organisation Mk 3.0 Climate System (CSIRO Mk3.0, hereafter CSIRO)].

Next we look at the vertical structures of the 40-day mode. Figure 9 shows the vertical structure of temperature for observation (NCEP reanalysis) and seven models with three-dimensional data available. Note that for four models the 3D data is available only below 200 mb. In observation, the 40-day mode displays a two-layer structure during the precipitating phase, with a cold core between surface and 250 mb, and a warm core above 250 mb. Five of the seven models (GFDL2.0, GFDL2.1, CGCM, MPI, and CNRM) reproduce the two-layer structure. In GISS-AOM the two-layer structure is shifted to the later phase by about 7 days. MRI simulates a cold core between 200 and 850 mb, and a warm core below 850 mb.

Figure 10 shows the vertical structure of geopotential height. Consistent with the temperature structure, the observed geopotential height displays a deep barotropic structure, with negative anomaly extending from the surface to 100 mb during the precipitating phase (Fig. 10a).

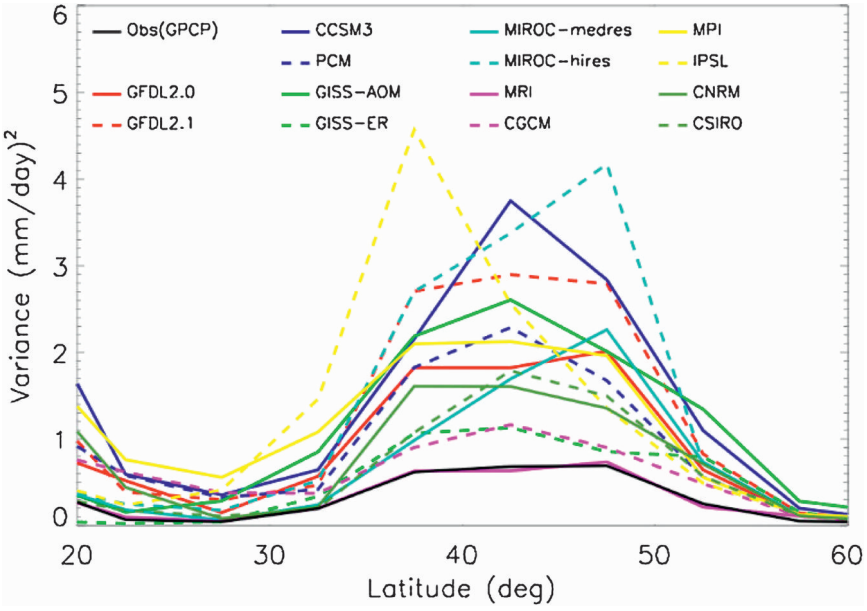

FIG. 7. As in Fig. 5, but for the variance of the 40-day mode.

All models reproduce the deep barotropic structure. However, in four models the correlation is low in the upper troposphere (GFDL2.1, GISS-AOM, MRI, and MPI).

Figure 11 shows the vertical structure of divergence. The observed divergence displays a two-layer structure during the precipitating phase, with convergence from the surface to 650 mb, and divergence above 650 mb (Fig. 11a). All but one model (MPI) reproduce fairly well the two-layer structure, although in GISS-AOM (Fig. 11d) the convergence layer is too deep, extending from the surface to 450 mb.

Next we look at the teleconnection pattern associated with the 40-day mode. Figure 12 shows the linear correlation of the 40-day-mode precipitation anomaly versus itself averaged between 35° and 40°N, 125° and 115°W. In observation (Fig. 12a), there is a three-cell pattern with positive precipitation anomaly over the western United States and negative anomalies over the eastern Pacific and the Pacific Northwest. At the same time, there is a dipole over the tropical Pacific with positive anomaly in the central Pacific and negative anomaly in the western Pacific. These are consistent with the results of Mo (1999, her Fig. 5c), who demonstrated that the dipole over the tropical Pacific is associated with the MJO. Most of the models simulate to some extent the three-cell pattern around the western United States. However, only two models (CCSM3 and PCM) simulate the dipole over the tropical Pacific. Four other models (GISS-AOM, GISS-ER, MIROC-medres, and MIROC-hires) produce statistically significant positive anomaly in the central Pacific but no statistically significant negative anomaly in western Pacific.

To summarize, the models tend to simulate overly large variance of the 40-day mode over the western United States and Canada. All models with three-dimensional data available reproduce the deep barotropic structure of the 40-day mode. All models reproduce to some extent the three-cell pattern of precipitation anomaly around the western United States, but only five models capture the northward propagation, and only two models simulate the teleconnection with the MJO in tropical Pacific.

e. *The 22-day mode*

Figure 13 shows the meridional profile of the 22-day mode variance averaged between 125° and 115°W. For both the observation and the models, the spatial distribution of the 22-day mode variance looks quite similar to that of the total intraseasonal variance and the 40-day mode. Eleven of the 14 models (GFDL2.0, GFDL2.1, CCSM3, PCM, GISS-AOM, MIROC-medres, MIROC-hires, CGCM, MPI, IPSL, and CSIRO) produce more than 2 times the observed 22-day mode variance over the western United States and Canada, while 3 models (MRI, CNRM, and GISS-ER) produce variances that are very close to the observed value.

Figure 14 shows the lag-correlation of the 22-day-mode precipitation anomaly averaged between 125° and 115°W with respect to itself at 37.5°N, 240°E. In observation (Fig. 14a), the 22-day mode propagates northward from the equator to 45°N, which is consistent with the results of Mo (1999). Nine of the 14 models simulate coherent northward propagation (GFDL2.0, GFDL2.1,

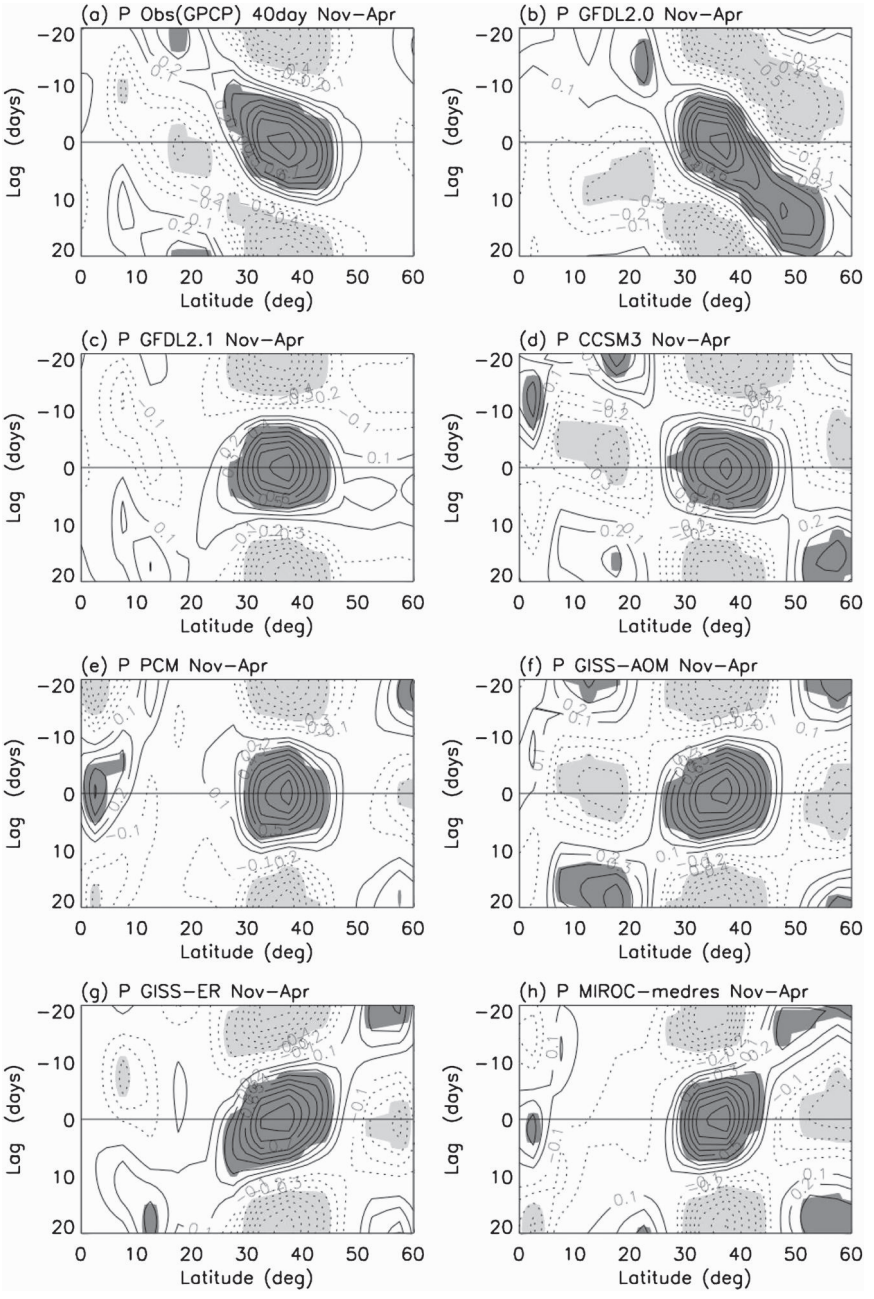

FIG. 8. Lag-correlation of the 40-day-mode precipitation anomaly averaged between 235° and 245°E with respect to itself at 37.5°N, 240°E for the 14 IPCC AR4 models. Shading denotes the regions where lag-correlation is above the 95% confidence level.

CCSM3, GISS-ER, MIROC-hires, MRI, CGCM, MPI, and CSIRO). Three models produce standing oscillation (GFDL2.1, GISS-AOM, and CNRM), one model simulates southward propagation (PCM), and two models display different propagation direction in different regions (MIROC-medres and IPSL).

Figure 15 shows the teleconnection pattern of the 22-day mode. In observation (Fig. 15a), there is a positive anomaly extending from western United States to 15°N, 210°E, a positive anomaly around 15°S, 210°E, and a negative anomaly around 15°N, 130°E. Nine of the 14 models reproduce a statistically significant positive anomaly around 15°N, 210°E (GFDL2.0, CCSM3, GISS-AOM, GISS-ER, MIROC-medres, MIROC-hires, IPSL, CNRM, and CSIRO), although in some models it is shifted slightly northward (e.g., GFDL2.0 and CCSM3).

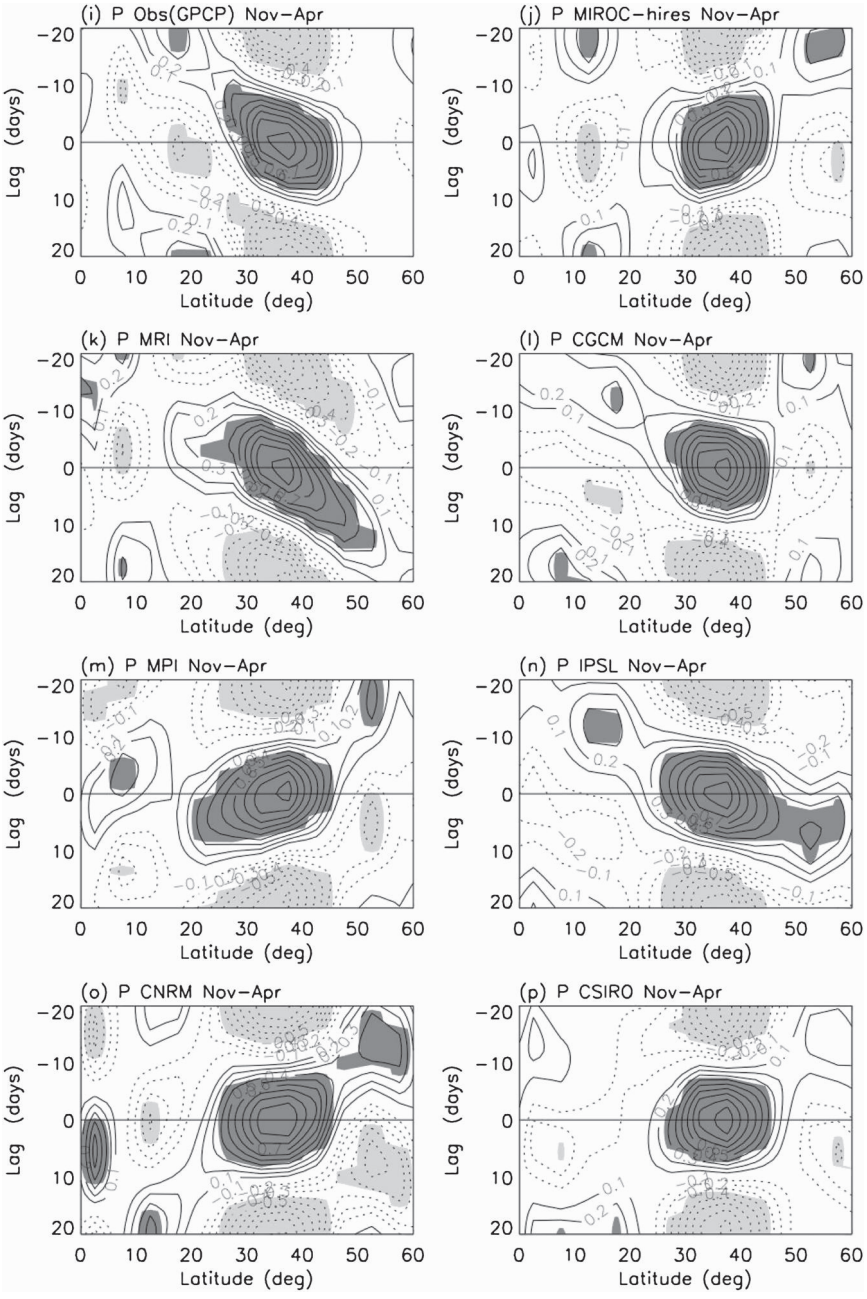

FIG. 8. (*Continued*)

Three models reproduce a statistically significant positive anomaly around 15°S, 210°E (MIROC-hires, CSIRO, and GFDL2.1), and only one model simulates a statistically significant negative anomaly around 15°N, 130°E (CSIRO).

5. Summary and discussion

This study evaluates the intraseasonal variation of winter precipitation over the western United States in 14 IPCC AR4 coupled GCMs. The results show that the models tend to overestimate the northern winter (November–April) seasonal mean precipitation over the western United States and Canada. The models also tend to produce overly strong intraseasonal variability in western U.S. wintertime precipitation, in spite of the overly weak tropical intraseasonal variability in most of the models. All models capture both the 40-day mode and the 22-day mode, usually with overly large variances. For the 40-day mode, models tend to reproduce its deep

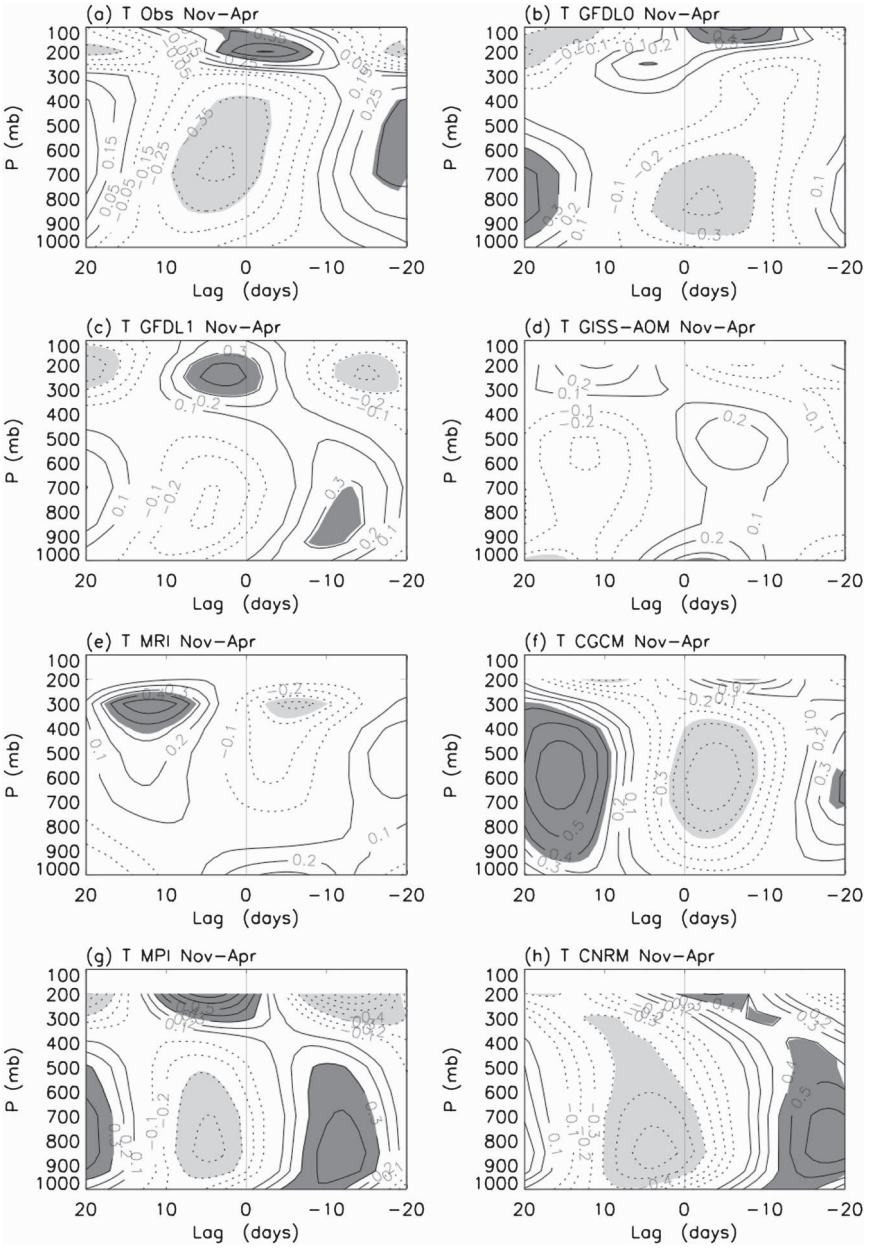

FIG. 9. Lag-correlation of temperature averaged between 30°–°N, 125°–115°W vs the 40-day-mode precipitation anomaly at the same location for observation (NCEP reanalysis) and seven models. Shading denotes the area where correlation is above the 95% confidence level, with dark (light) shading for positive (negative) correlation.

barotropic vertical structure and three-cell horizontal structure, but only 5 of the 14 models capture its northward propagation, and only 2 models simulate its teleconnection with the Madden–Julian oscillation in the tropical Pacific. For the 22-day mode, 8 of the 14 models reproduce its coherent northward propagation, and 9 models capture its teleconnection with precipitation in the tropical Pacific.

The above results have two implications on the dynamics of intraseasonal variability of western U.S. winter precipitation. First, in spite of the lack of MJO and overly weak tropical intraseasonal variability in most of the models, they still produce overly strong intraseasonal variability of western U.S. winter precipitation, suggesting that tropical forcing may be a secondary mechanism for generating this variability. This is consistent

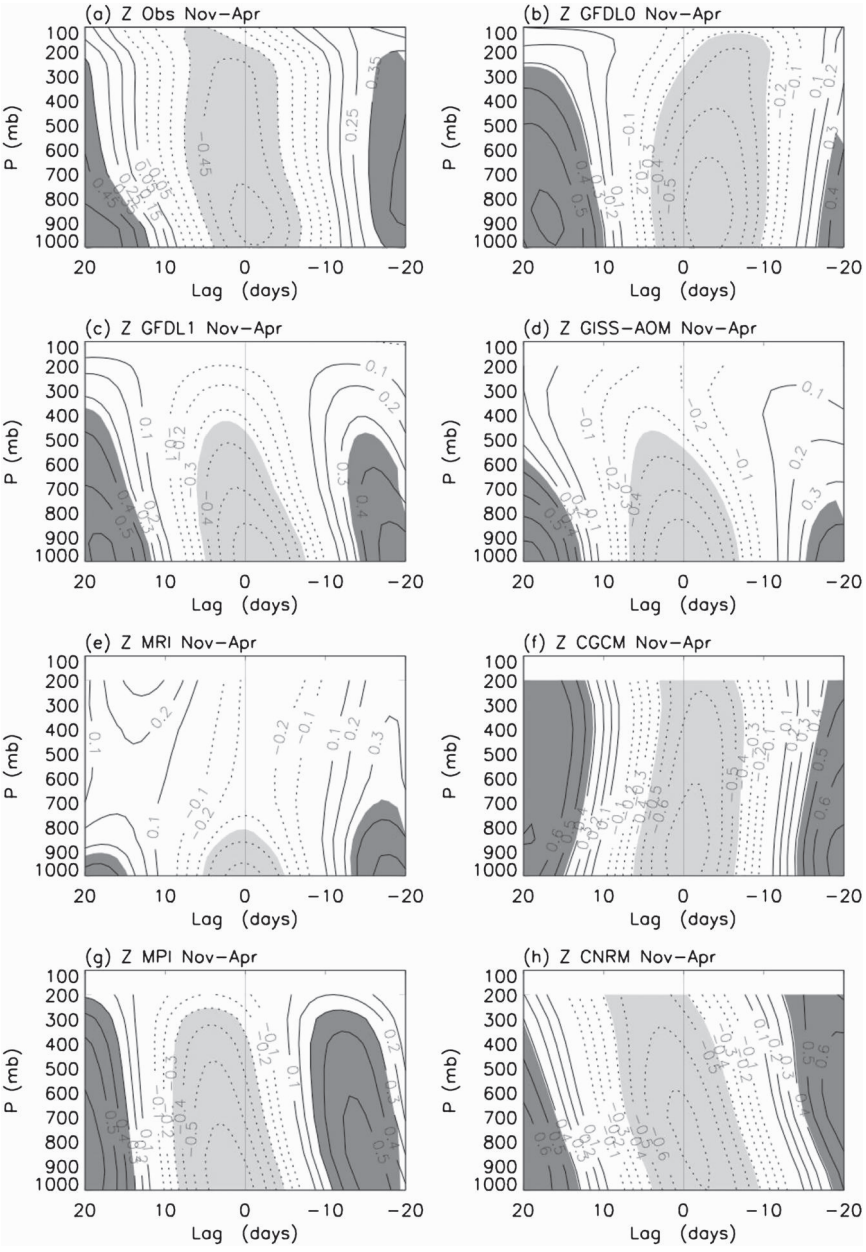

FIG. 10. As in Fig. 9, but for geopotential height.

with several previous studies (e.g., Lau 1981; Simmons et al. 1983; Karoly et al. 1989; Schubert and Park 1991; Schubert et al. 1993).

Second, a new finding of this study is that several models could reproduce the northward propagation of the 40-day mode with the lack of MJO signals in those models. This suggests that the northward propagation of the 40-day mode may not be generated by the Rossby wave emanation from the tropical MJO. Theoretical and observational studies have suggested several different mechanisms for northward propagation of intraseasonal modes, including land surface heat flux (Webster 1983; Srinivasan et al. 1993), ocean surface sensible heat flux (Hsu et al. 2004), vertical-shear-induced boundary layer moisture convergence (Jiang et al. 2004), and moisture advection (Jiang et al. 2004). In future studies, analyses of heat, moisture, and vorticity budgets are needed to examine if these mechanisms contribute to the northward propagations in the models.

Among the 14 coupled GCMs, the MRI model arguably produces the best overall intraseasonal variability of western U.S. winter precipitation. This is likely associated

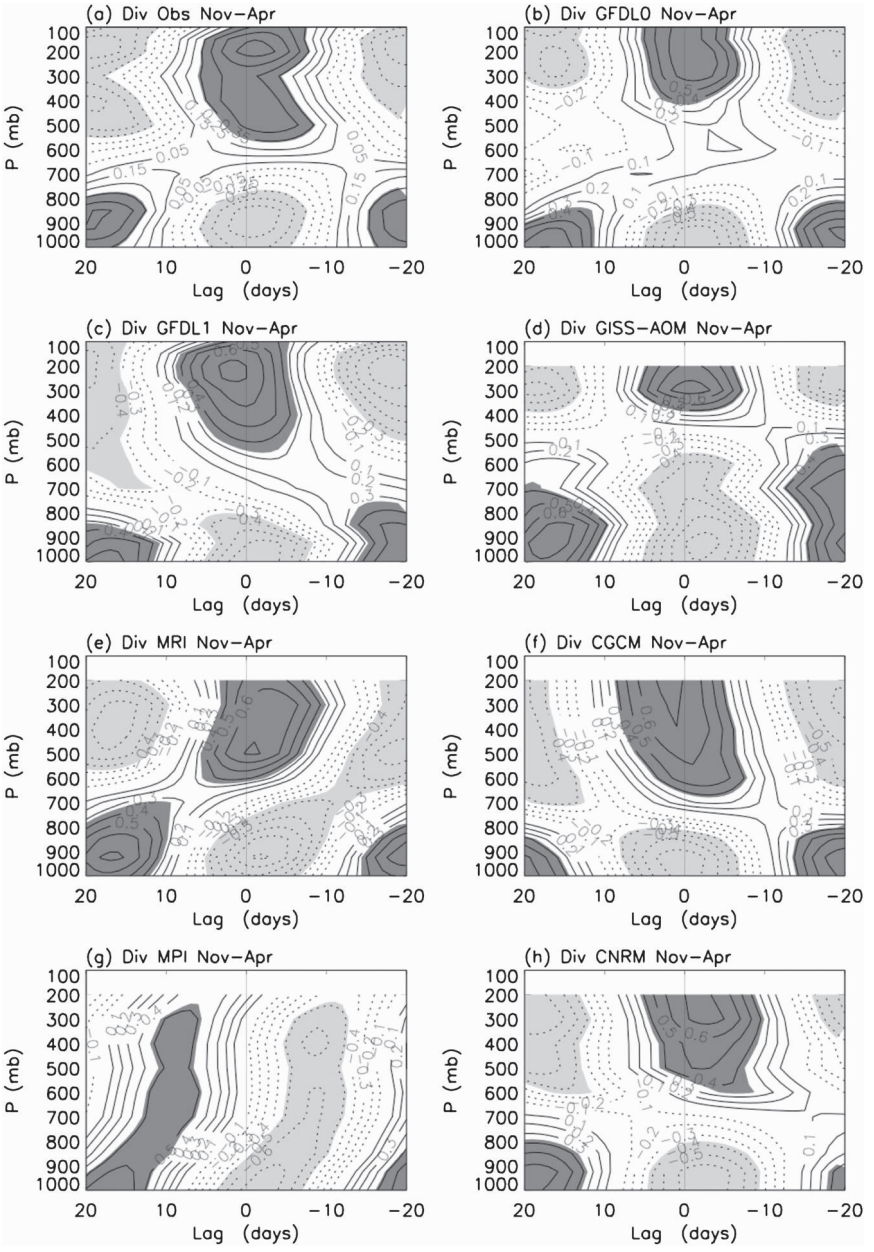

FIG. 11. As in Fig. 9, but for divergence.

with its good simulation of the wintertime seasonal mean precipitation, because our results show that the models' intraseasonal variability generally increases with the increase of seasonal mean precipitation. However, one major caveat of this evaluation is the uncertainties associated with the precipitation observations, which are discussed briefly in section 2. Therefore we must be cautious when giving any ranking to the models' simulations. Currently, NASA is planning its Global Precipitation Measurement (GPM) Mission to improve our measurements of precipitation over both the tropics and extratropics. We expect that the next generation of precipitation analysis will provide a more solid benchmark for evaluating the climate model simulations.

Acknowledgments. Gary Russell kindly provided a detailed description of the GISS-AOM model. We acknowledge the international modeling groups for providing their data for analysis, the Program for Climate Model Diagnosis and Intercomparison (PCMDI) for collecting and archiving the model data, the JSC/CLIVAR

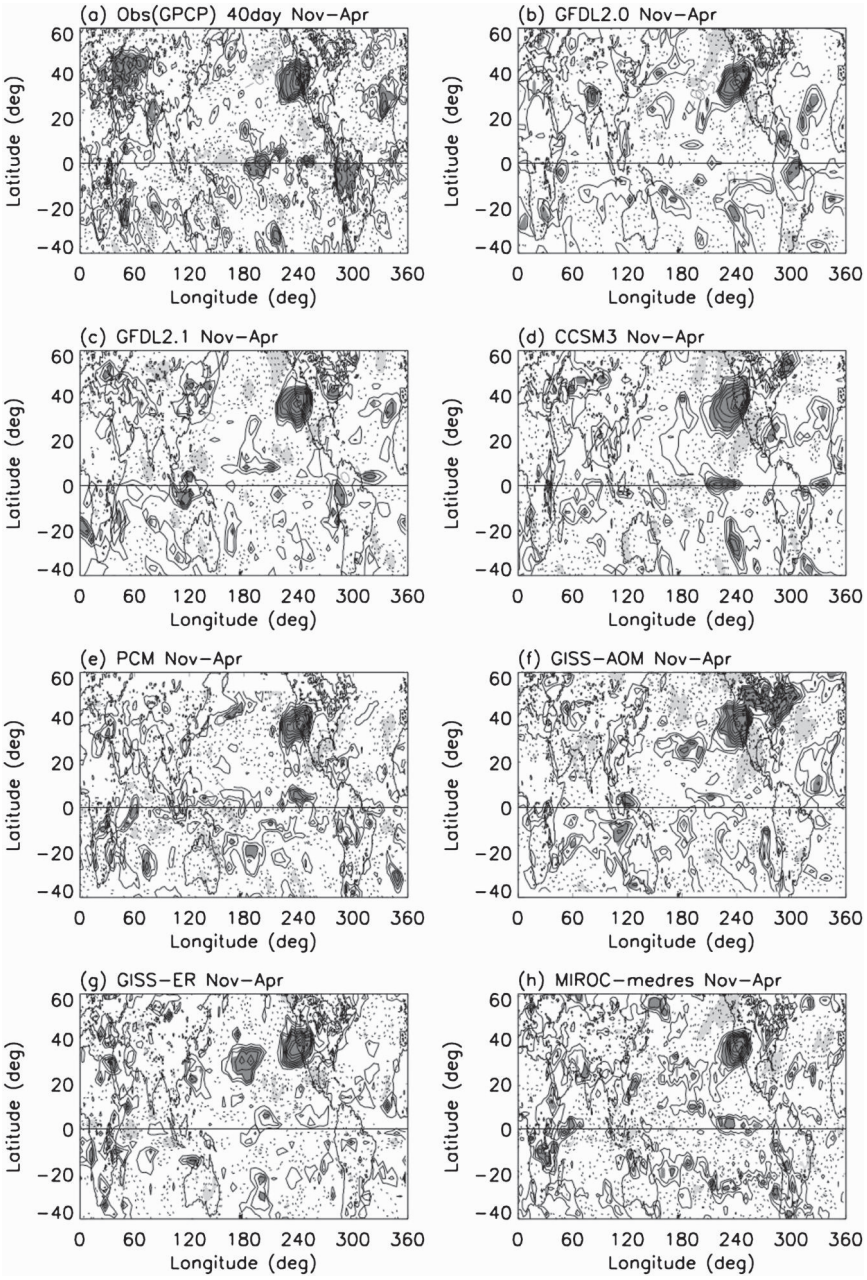

FIG. 12. Linear correlation of the 40-day-mode precipitation anomaly vs itself averaged between 35°–40°N, 125°–115°W for the 14 models. Shading denotes the area where correlation is above the 95% confidence level, with dark (light) shading for positive (negative) correlation.

Working Group on Coupled Modeling (WGCM) and their Coupled Model Intercomparison Project (CMIP) and Climate Simulation Panel for organizing the model data analysis activity, and the IPCC WG1 TSU for technical support. The IPCC Data Archive at Lawrence Livermore National Laboratory is supported by the Office of Science, U.S. Department of Energy. J. L. Lin was supported by the NASA MAP Program and NSF Grant ATM-0745872. T. Shinoda was supported by NSF Grants OCE-0453046 and ATM-0745897, the NOAA CPO/CVP program, and the 6.1 project Global Remote Littoral Forcing via Deep Water Pathways sponsored by the Office of Naval Research (ONR) under Program Element 601153N.

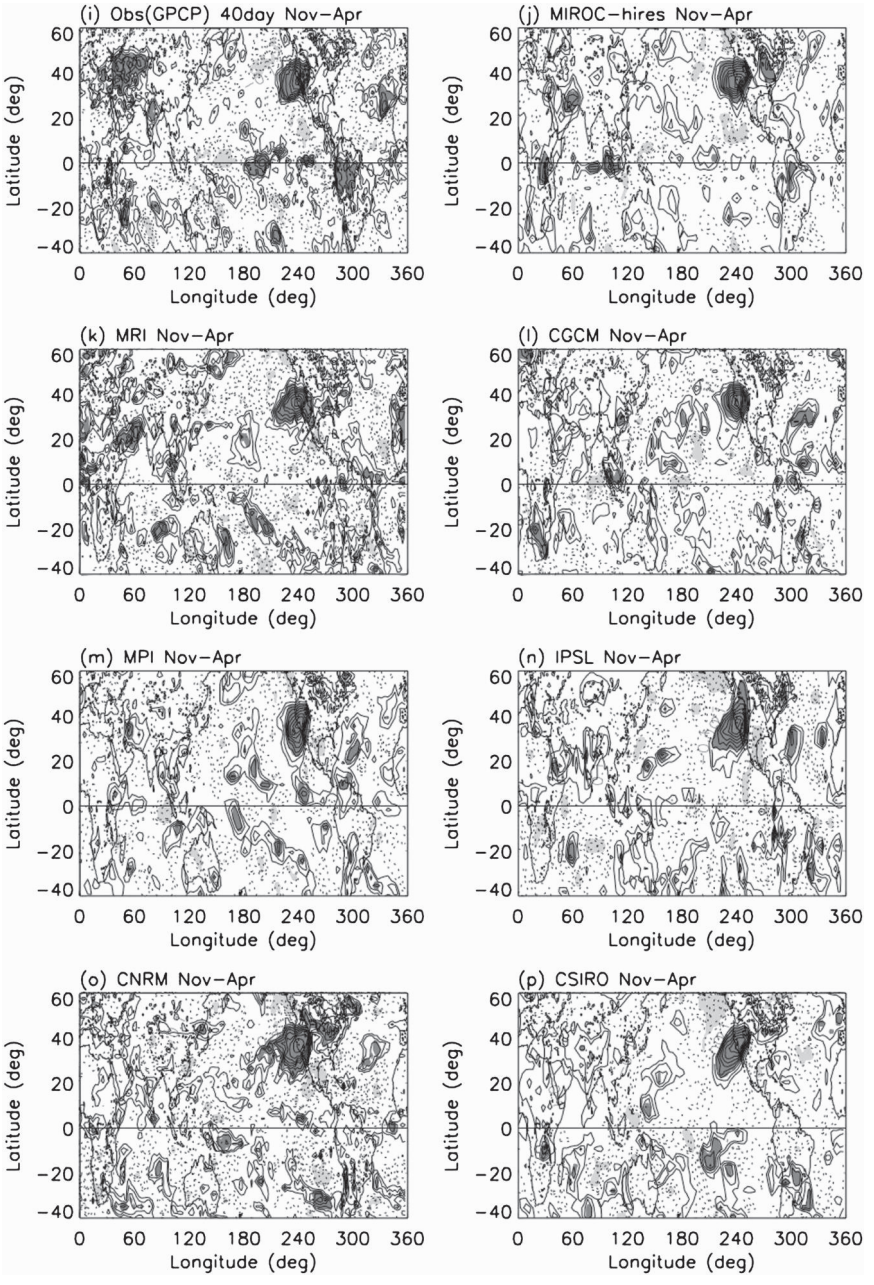

FIG. 12. (*Continued*)

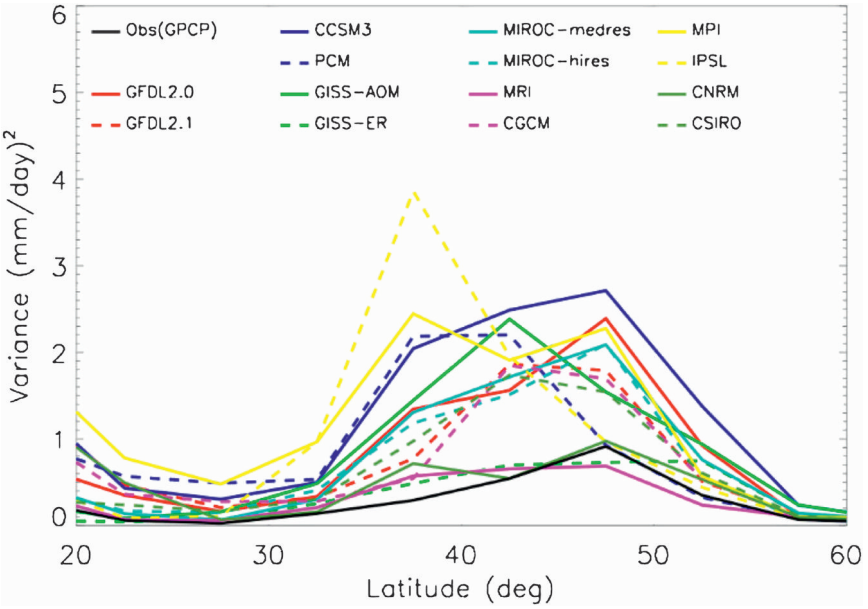

FIG. 13. As in Fig. 5, but for the variance of the 22-day mode.

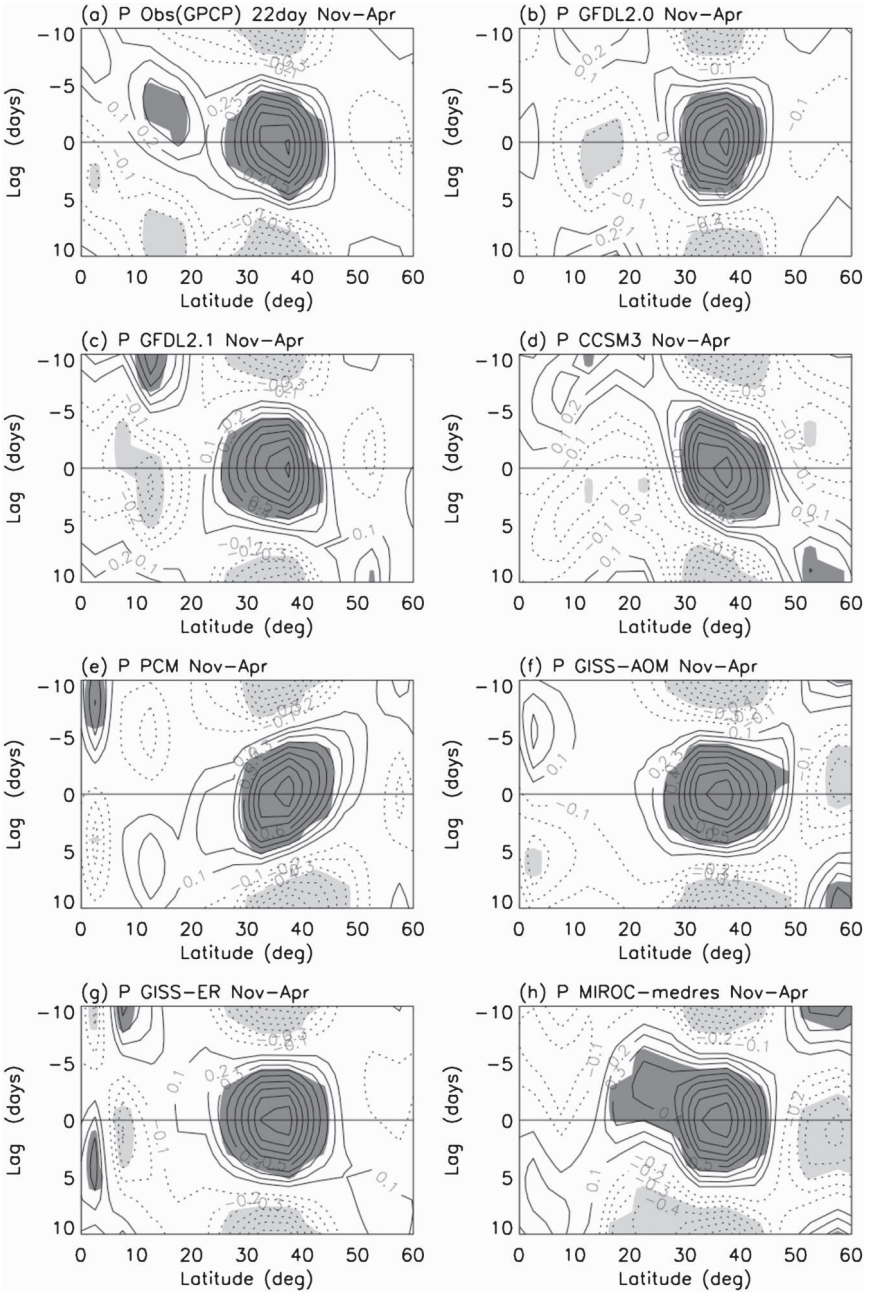

FIG. 14. Lag-correlation of the 22-day-mode precipitation anomaly averaged between 125° and 115°W with respect to itself at 37.5°N, 120°W for the 14 models. Shading denotes the regions where lag-correlation is above the 95% confidence level.

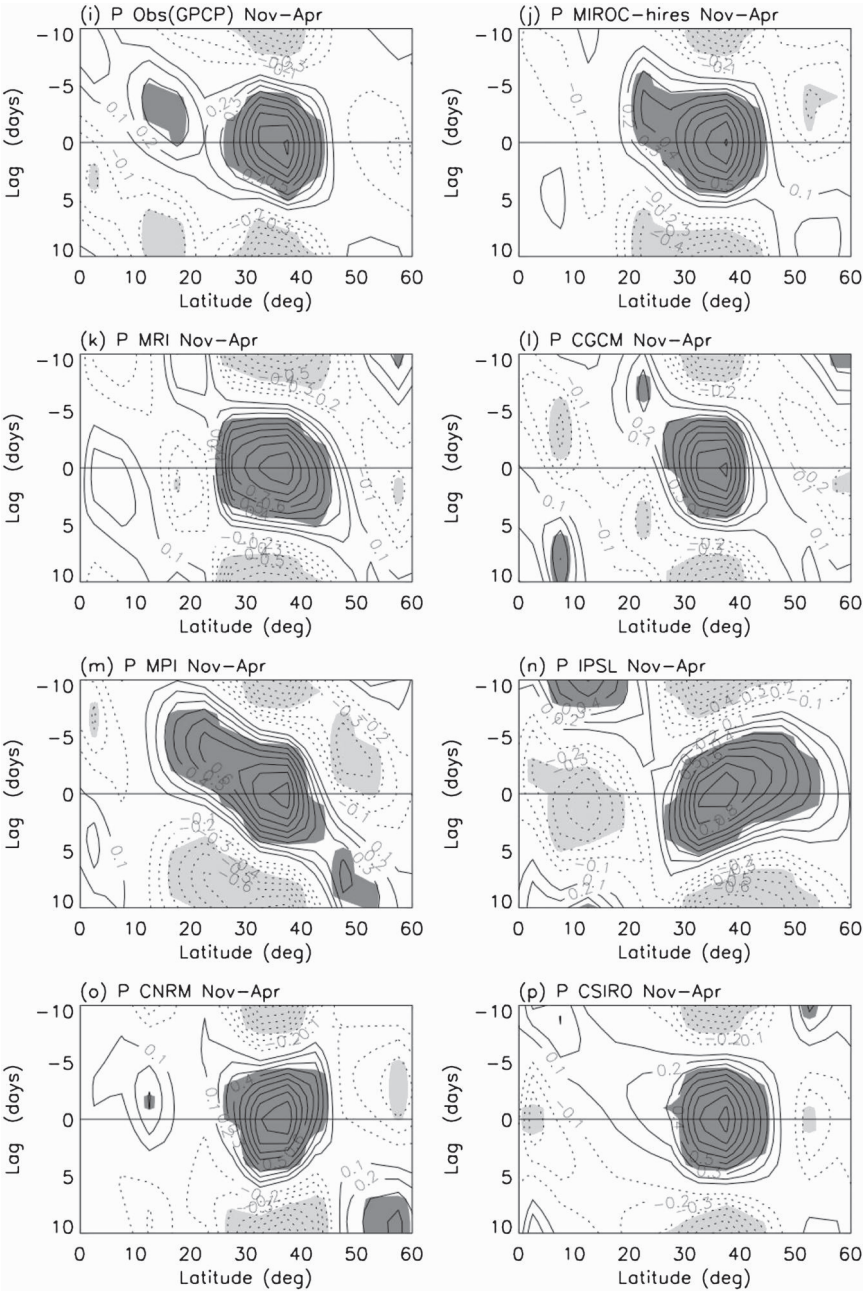

FIG. 14. (*Continued*)

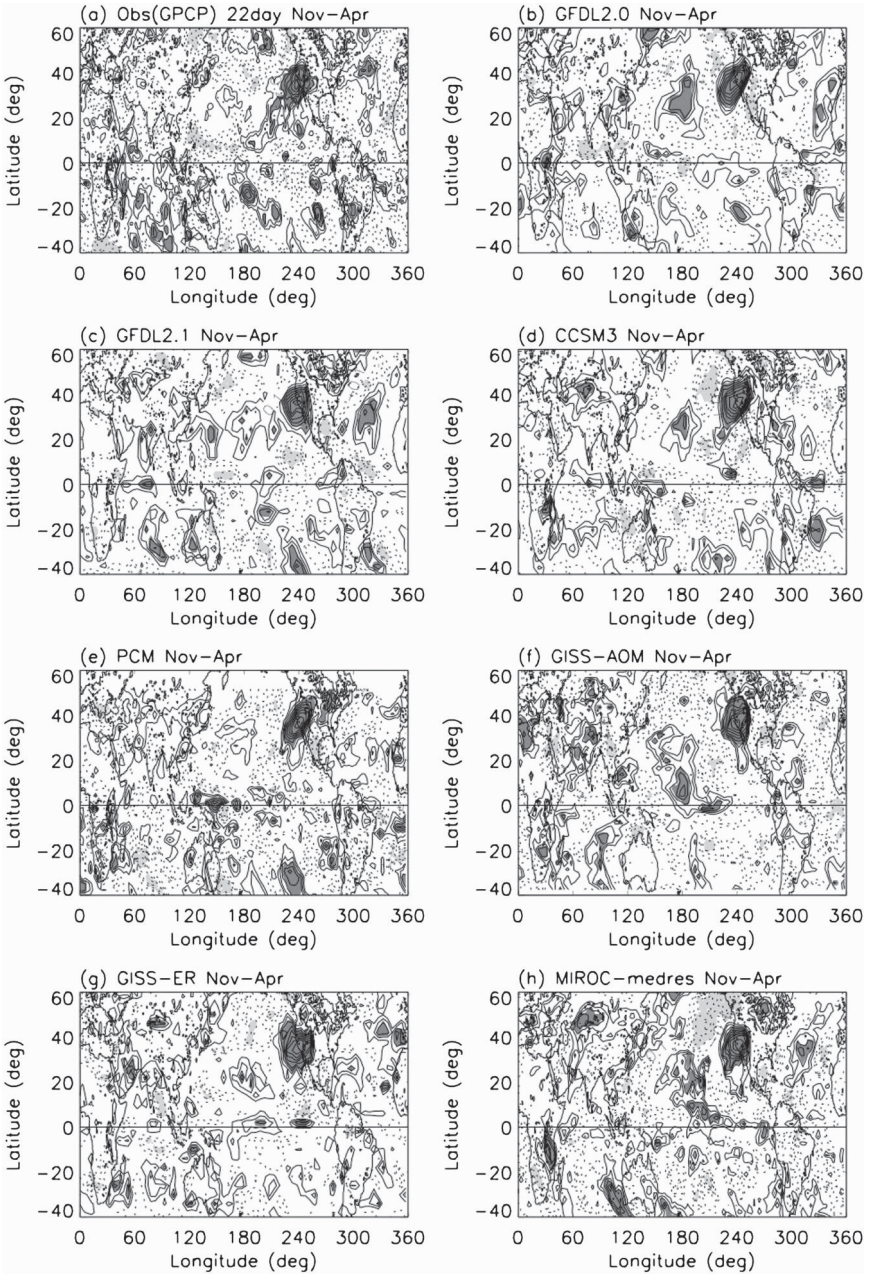

FIG. 15. As in Fig. 12, but for the 22-day mode.

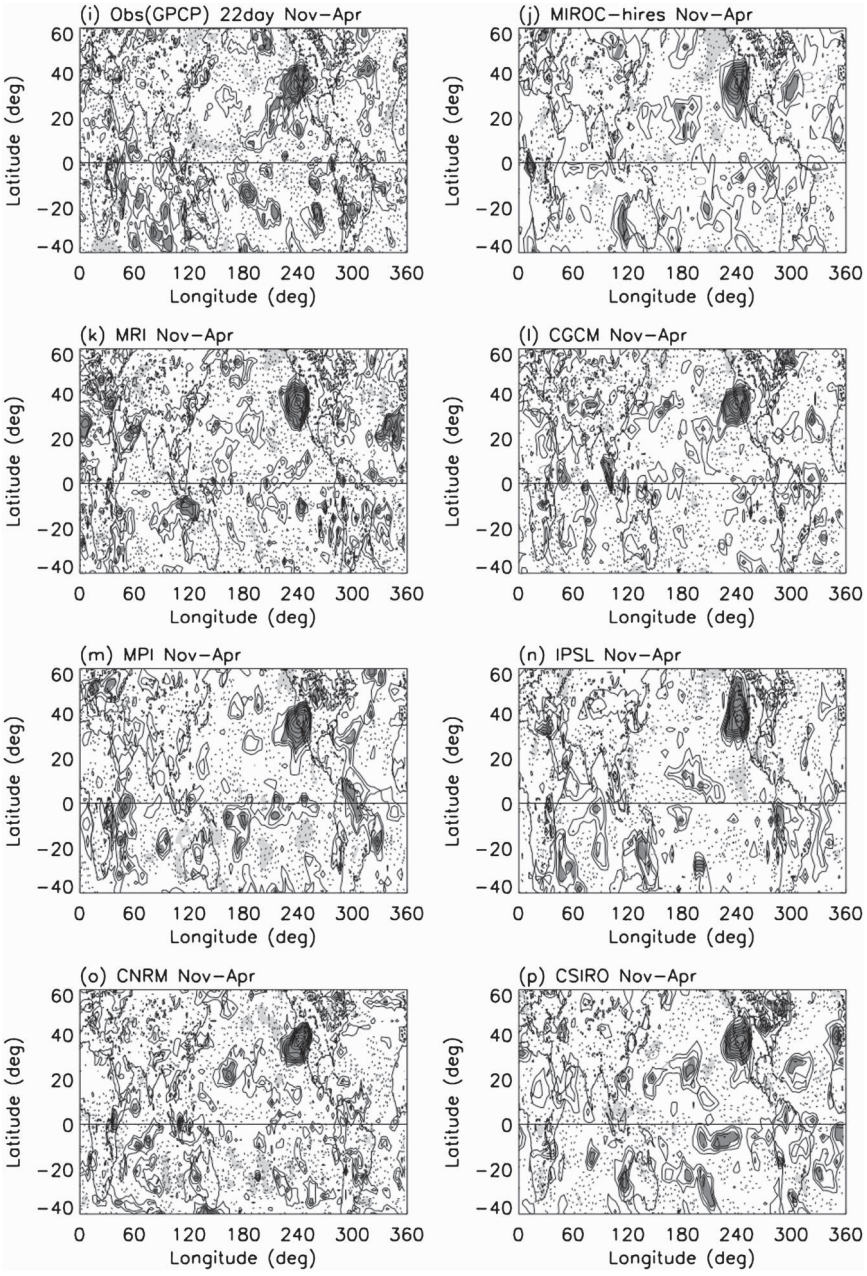

FIG. 15. (*Continued*)

REFERENCES

Bougeault, P., 1985: A simple parameterization of the large-scale effects of cumulus convection. *Mon. Wea. Rev.,* **113,** 2108–2121.

Branstator, G., 1987: A striking example of the atmosphere's leading traveling pattern. *J. Atmos. Sci.,* **44,** 2310–2323.

Carr, M. T., and C. S. Bretherton, 2001: Convective momentum transport over the tropical Pacific: Budget estimates. *J. Atmos. Sci.,* **58,** 1673–1693.

Del Genio, A. D., and M.-S. Yao, 1993: Efficient cumulus parameterization for long-term climate studies: The GISS scheme. *The Representation of Cumulus Convection in Numerical Models, Meteor. Monogr.,* No. 46, Amer. Meteor. Soc., 181–184.

Dole, R. M., and R. X. Black, 1990: Life cycles of persistent anomalies. Part II: The development of persistent negative height anomalies over the North Pacific Ocean. *Mon. Wea. Rev.,* **118,** 824–846.

Duchan, C. E., 1979: Lanczos filtering in one and two dimensions. *J. Appl. Meteor.,* **18,** 1016–1022.

Emanuel, K. A., 1991: A scheme for representing cumulus convection in large-scale models. *J. Atmos. Sci.,* **48,** 2313–2329.

Emori, S., T. Nozawa, A. Numaguti, and I. Uno, 2001: Importance of cumulus parameterization for precipitation simulation over East Asia in June. *J. Meteor. Soc. Japan,* **79,** 939–947.

Frederiksen, J. S., 1986: Instability theory and nonlinear evolution of blocks and mature anomalies. *Advances in Geophysics,* Vol. 29, Academic Press, 277–303.

Gregory, D., and P. R. Rowntree, 1990: A mass flux convection scheme with representation of cloud ensemble characteristics and stability-dependent closure. *Mon. Wea. Rev.,* **118,** 1483–1506.

Gruber, A., and V. Levizzani, 2008: Assessment of global precipitation products. A project of the World Climate Research Programme Global Energy and Water Cycle Experiment (GEWEX) Radiation Panel. WCRP Rep. 128, WMO/TD 1430, 57 pp.

Held, I. M., S. W. Lyons, and S. Nigam, 1989: Transients and the extratropical response to El Niño. *J. Atmos. Sci.,* **46,** 163–174.

Hsu, H.-H., C.-H. Weng, and C.-H. Wu, 2004: Contrasting characteristics between the northward and eastward propagation of the intraseasonal oscillation during the boreal summer. *J. Climate,* **17,** 727–743.

Huffman, G. J., R. F. Adler, M. M. Morrissey, D. T. Bolvin, S. Curtis, R. Joyce, B. McGavock, and J. Susskind, 2001: Global precipitation at one-degree daily resolution from multisatellite observations. *J. Hydrometeor.,* **2,** 36–50.

Jiang, X., T. Li, and B. Wang, 2004: Structures and mechanisms of the northward propagating boreal summer intraseasonal oscillation. *J. Climate,* **17,** 1022–1039.

Kalnay, E., and Coauthors, 1996: The NCEP/NCAR 40-Year Reanalysis Project. *Bull. Amer. Meteor. Soc.,* **77,** 437–471.

Karoly, D. J., R. A. Plumb, and M. Ting, 1989: Examples of horizontal propagation of quasi-stationary waves. *J. Atmos. Sci.,* **46,** 2802–2811.

Knutson, T. R., and K. M. Weickmann, 1987: 30–60 day atmospheric oscillations: Composite life cycles of convection and circulation anomalies. *Mon. Wea. Rev.,* **115,** 1407–1436.

Kuo, H.-L., 1974: Further studies of the parameterization of the influence of cumulus convection on large-scale flow. *J. Atmos. Sci.,* **31,** 1232–1240.

Lau, K. M., 1981: Oscillations in a simple equatorial climate system. *J. Atmos. Sci.,* **38,** 248–261.

Lau, N.-C., 1988: Variability of the observed midlatitude storm tracks in relation to low-frequency changes in the circulation pattern. *J. Atmos. Sci.,* **45,** 2718–2743.

Lin, J. L., M. H. Zhang, and B. E. Mapes, 2005: Zonal momentum budget of the Madden–Julian oscillation: The sources and strength of equivalent linear damping. *J. Atmos. Sci.,* **62,** 2172–2188.

——, and Coauthors, 2006: Tropical intraseasonal variability in 14 IPCC AR4 climate models. Part I: Convective signals. *J. Climate,* **19,** 2665–2690.

——, B. E. Mapes, and W. Han, 2008: What are the sources of mechanical damping in Matsuno–Gill type models? *J. Climate,* **21,** 165–179.

Mak, M., 1995: Orthogonal wavelet analysis: Interannual variability in the sea surface temperature. *Bull. Amer. Meteor. Soc.,* **76,** 2179–2186.

Marcus, S. L., M. Ghil, and J. O. Dickey, 1994: The extratropical 40-day oscillation in the UCLA general circulation model. Part I: Atmospheric angular momentum. *J. Atmos. Sci.,* **51,** 1431–1446.

——, ——, and ——, 1996: The extratropical 40-day oscillation in the UCLA general circulation model. Part II: Spatial structure. *J. Atmos. Sci.,* **53,** 1993–2014.

Mo, K. C., 1999: Alternating wet and dry episodes over California and intraseasonal oscillations. *Mon. Wea. Rev.,* **127,** 2759–2776.

——, and R. W. Higgins, 1998a: Tropical influences on California precipitation. *J. Climate,* **11,** 412–430.

——, and ——, 1998b: Tropical convection and precipitation regimes in the western United States. *J. Climate,* **11,** 2404–2423.

——, and J. Nogues-Paegle, 2005: Pan-America. *Intraseasonal Variability in the Atmosphere–Ocean Climate System,* W. K. M. Lau and D. Waliser, Eds., Springer-Praxis, 95–124.

Moorthi, S., and M. J. Suarez, 1992: Relaxed Arakawa–Schubert: A parameterization of moist convection for general circulation models. *Mon. Wea. Rev.,* **120,** 978–1002.

Murakami, M., 1979: Large-scale aspects of deep convective activity over the GATE area. *Mon. Wea. Rev.,* **107,** 994–1013.

Nordeng, T. E., 1994: Extended versions of the convective parameterization scheme at ECMWF and their impact on the mean and transient activity of the model in the tropics. ECMWF Tech. Memo. 206, 41 pp.

Pan, D.-M., and D. A. Randall, 1998: A cumulus parameterization with a prognostic closure. *Quart. J. Roy. Meteor. Soc.,* **124,** 949–981.

Randall, D. A., and Coauthors, 2007: Climate models and their evaluation. *Climate Change 2007: The Physical Science Basis,* S. Solomon et al., Eds., Cambridge University Press, 589–662.

Russell, G. L., J. R. Miller, and D. Rind, 1995: A coupled atmosphere–ocean model for transient climate change studies. *Atmos.–Ocean,* **33,** 683–730.

Schubert, S. D., 1986: The structure, energetics and evolution of the dominant frequency-dependent three-dimensional atmospheric modes. *J. Atmos. Sci.,* **43,** 1210–1237.

——, and C. K. Park, 1991: Low-frequency intraseasonal tropical–extratropical interactions. *J. Atmos. Sci.,* **48,** 629–650.

——, M. Suarez, C. K. Park, and S. Moorthi, 1993: GCM simulations of intraseasonal variability in the Pacific/North American region. *J. Atmos. Sci.,* **50,** 1991–2007.

Simmons, A. J., J. M. Wallace, and G. W. Branstator, 1983: Barotropic wave propagation and instability, and atmospheric teleconnection patterns. *J. Atmos. Sci.,* **40,** 1363–1392.

Srinivasan, J., S. Gadgil, and P. J. Webster, 1993: Meridional propagation of large-scale monsoon convective zones. *Meteor. Atmos. Phys.,* **52,** 15–35.

Tiedke, M., 1989: A comprehensive mass flux scheme for cumulus parameterization in large-scale models. *Mon. Wea. Rev.,* **117,** 1779–1800.

Tokioka, T., K. Yamazaki, A. Kitoh, and T. Ose, 1988: The equatorial 30–60-day oscillation and the Arakawa–Schubert penetrative cumulus parameterization. *J. Meteor. Soc. Japan,* **66,** 883–901.

Torrence, C., and G. P. Compo, 1998: A practical guide to wavelet analysis. *Bull. Amer. Meteor. Soc.,* **79,** 61–78.

Wallace, J. M., and D. S. Gutzler, 1981: Teleconnections in the geopotential height field during the Northern Hemisphere winter. *Mon. Wea. Rev.,* **109,** 784–812.

Webster, P. J., 1983: Mechanisms of monsoon low-frequency variability: Surface hydrological effects. *J. Atmos. Sci.,* **40,** 2110–2124.

Weickmann, K. M., G. R. Lussky, and J. E. Kutzbach, 1985: Intraseasonal (30–60 day) fluctuations of outgoing longwave radiation and 250 mb streamfunction during northern winter. *Mon. Wea. Rev.,* **113,** 941–961.

Wheeler, M., and G. N. Kiladis, 1999: Convectively coupled equatorial waves: Analysis of clouds and temperature in the wavenumber–frequency domain. *J. Atmos. Sci.,* **56,** 374–399.

Zhang, G. J., and N. A. McFarlane, 1995: Sensitivity of climate simulations to the parameterization of cumulus convection in the CCC-GCM. *Atmos.–Ocean,* **3,** 407–446.